Chemical
Science

EDGE ARTICLE

View Article Online
View Journal | View Issue

Cite this: *Chem. Sci.*, 2023, **14**, 5379

All publication charges for this article have been paid for by the Royal Society of Chemistry

Received 3rd March 2023
Accepted 14th April 2023

DOI: 10.1039/d3sc01163a

rsc.li/chemical-science

The promotional role of Mn in CO_2 hydrogenation over Rh-based catalysts from a surface organometallic chemistry approach†

Wei Zhou, Scott R. Docherty, Christian Ehinger, Xiaoyu Zhou and Christophe Copéret *

Rh-based catalysts modified by transition metals have been intensively studied for CO_2 hydrogenation due to their high activity. However, understanding the role of promoters at the molecular level remains challenging due to the ill-defined structure of heterogeneous catalysts. Here, we constructed well-defined $RhMn@SiO_2$ and $Rh@SiO_2$ model catalysts *via* surface organometallic chemistry combined with thermolytic molecular precursor (SOMC/TMP) approach to rationalize the promotional effect of Mn in CO_2 hydrogenation. We show that the addition of Mn shifts the products from almost pure CH_4 to a mixture of methane and oxygenates (CO, CH_3OH, and CH_3CH_2OH) upon going from $Rh@SiO_2$ to $RhMn@SiO_2$. *In situ* X-ray absorption spectroscopy (XAS) confirms that the Mn^{II} is atomically dispersed in the vicinity of metallic Rh nanoparticles and enables to induce the oxidation of Rh to form the Mn–O–Rh interface under reaction conditions. The formed interface is proposed to be key to maintaining Rh^+ sites, which is related to suppressing the methanation reaction and stabilizing the formate species as evidenced by *in situ* DRIFTS to promote the formation of CO and alcohols.

Introduction

The continuous increase in the concentration of atmospheric CO_2 has been raising serious concerns due to its visible environmental impact associated with the greenhouse effect and ocean acidification.[1,2] CO_2 hydrogenation using renewable H_2 represents one of the most promising strategies to mitigate CO_2 emission and realize carbon neutrality.[3,4] Among numerous catalysts employed for CO_2 hydrogenation, rhodium-based catalysts have drawn continued interest due to their high activity.[5,6] In general, methanation dominates over Rh-based catalysts, yielding methane as the main product. However, to steer product selectivity towards oxygenates, promoters such as Mn and Fe have been intensively investigated.[7–11] However, understanding the role of these promoters at the molecular level has been challenging due to the ill-defined structure of these catalysts. To address the complex structure of heterogeneous catalysts, surface organometallic chemistry combined with thermolytic molecular precursors (SOMC/TMP) has emerged as a promising approach to construct well-defined model catalysts with tailored composition and interfaces.[12,13] This approach results in materials that are more amenable to molecular-level spectroscopic characterization, hence they can be used to bridge the gap in understanding between complex heterogeneous systems and model catalysts, by enabling the development of detailed structure–activity relationships.

Our group has successfully applied this approach to various heterogeneous reactions such as the selective oxidation of methane[14] and propane dehydrogenation[15,16] as well as the selective CO_2 hydrogenation to methanol.[17] For instance, a series of Cu-based catalysts doped with various metals ($Cu/M@SiO_2$, M = Ti, Zr, Hf, Nb, Ta, Zn, Ga) were synthesized *via* the SOMC/TMP approach.[18–23] Metal nanoparticles with a narrow particle size distribution, similar metal dispersion, tailored interfaces, and compositions enabled the investigation of the influence of discrete physicochemical properties (Lewis acidity and alloying) on CO_2 hydrogenation. These studies have shown that the presence of Lewis acid sites, originating from early transition-metal metal dopants, boosts the CH_3OH formation rate *via* the stabilization of formate and methoxy intermediates.[21] For the $Cu–Ga@SiO_2$ and $Cu–Zn@SiO_2$ model catalysts, alloy phases have been observed upon the reduction treatment.[19,20] The oxidation of Zn or Ga to form small oxide domains is however observed from these alloys under reaction conditions, thus maximizing the interface with metallic Cu. The high methanol selectivity in a wider range of CO_2 conversion is probably associated with such a dynamic process. Overall, the SOMC approach has opened new avenues to shed light on complex systems and to develop detailed structure–activity relationships, that can be transferred to other heterogeneous catalysts.

Department of Chemistry and Applied Bioscience, ETH Zürich, Vladimir Prelog Weg2, CH-8093 Zürich, Switzerland. E-mail: ccoperet@inorg.chem.ethz.ch

† Electronic supplementary information (ESI) available. CCDC 2237586 and 2237587. For ESI and crystallographic data in CIF or other electronic format see DOI: **https://doi.org/10.1039/d3sc01163a**

With this in mind, we synthesized well-defined RhMn@SiO_2 and Rh@SiO_2 catalysts using the SOMC/TMP approach to elucidate the promotional role of Mn in CO_2 hydrogenation. We found that the presence of Mn significantly suppresses methanation, while the product distribution shifts from almost pure CH_4 to a mixture of CH_4, CO, and CH_3OH along with small amounts of CH_3CH_2OH upon going from Rh@SiO_2 to RhMn@SiO_2. Detailed *in situ* studies show that the isolated Mn^{II} in the vicinity of Rh nanoparticles is key to suppressing methanation by inducing the oxidation of Rh.

Results and discussion

Catalyst preparation and characterization

We first developed a Rh precursor, amenable for grafting with easy removal of organic ligands during the nanoparticle formation, namely (*N*,*N*′-diisopropylacetamidinate)(1,5-cyclooctadiene)rhodium, abbreviated as Rh(COD)(DIA). This compound is prepared by reacting Li(DIA)(THF) (Fig. S1–S3†) with chloro(1,5-cyclooctadiene)rhodium(I) to produce Rh(COD)(DIA) in high yield (90%) (Fig. S4–S7†). Rh(COD)(DIA) reacts with $SiO_{2\text{-}700}$ (silica dehydroxylated at 700 °C) as evidenced by solution NMR, with complete consumption of the molecular precursor upon contacting with $SiO_{2\text{-}700}$ (Fig. S8†). IR spectroscopy of the resulting materials shows the disappearance of Si–OH at 3747 cm^{-1} and the concomitant appearance of C–H stretching (3100–2700 cm^{-1}) and bending (1500–1300 cm^{-1}) bands, C═C and C═N stretching bands (1600–1700 cm^{-1}), and N–H stretching band from secondary amine (a low-intensity peak at *ca.* 3250 cm^{-1}) (Fig. S9†). These results confirm that Rh(COD)(DIA) was grafted on SiO_2 *via* protonolysis with the surface silanols to generate Rh(COD)(DIA)@SiO_2 (Fig. S10†). Furthermore, ^{13}C cross-polarization magic-angle spinning (CP-MAS) NMR displays signals at 163, 72, 45, 30, 22, and 12 ppm, consistent with the grafting of the molecular precursor (Fig. S11†). Notably the signal for C-sp^2 carbon of amidinate shifts from 179 ppm to 163 ppm after grafting due to the cleavage of the Rh–N bond *via* protonolysis. Reduction at 400 °C under a H_2 atmosphere removes all the ligands according to IR spectroscopy (Fig. S9†). The resulting dark solid (denoted as Rh@SiO_2) suggests particle formation; transmission electron microscopy (TEM) analysis of Rh@SiO_2 shows a narrow distribution of Rh nanoparticles centered at 3.3 nm (Fig. S12†).

Based on these encouraging results, the corresponding RhMn bimetallic catalyst was prepared in a two-step SOMC/TMP process, involving first the generation of the well-defined isolated Mn^{II} sites dispersed on silica prepared *via* the combined SOMC/TMP approach.[24] This material, denoted as Mn^{II}@SiO_2 (1.45 wt% Mn, 0.79 Mn/nm^2), was first synthesized by grafting the $[Mn(OSi(O\textit{t}Bu)_3)_2]_2$ on $SiO_{2\text{-}700}$, followed by thermal treatment at 400 °C under vacuum (10^{-5} mbar, Fig. S13†). The presence of –OH in Mn^{II}@SiO_2 allows the introduction of Rh through a second grafting step using Rh(COD)(DIA) (Fig. 1a). IR spectroscopy was used to monitor the grafting process (Fig. 1b): grafting of Rh(COD)(DIA) on Mn^{II}@SiO_2 shows a decrease in intensity of the surface silanols and the appearance of similar IR bands as observed during grafting on silica (*vide supra*). Upon treatment under H_2 at 400 °C, all organic ligands are removed and the surface silanols are regenerated (Fig. 1b). This material is henceforth denoted as RhMn@SiO_2. TEM shows the formation of significantly smaller nanoparticles for RhMn@SiO_2 centered at 1.9 nm (Fig. 1c) when compared to monometallic Rh@SiO_2, which already suggests a substantial influence of Mn on the nanoparticle structure.

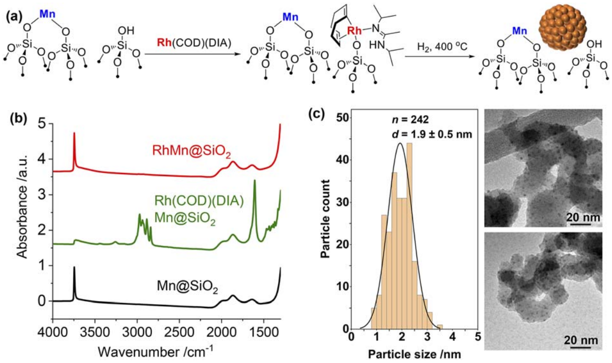

Fig. 1 (a) Schematic procedure for grafting of Rh(COD)(DIA) on Mn^{II}@SiO_2 followed by reduction under H_2 at 400 °C. (b) IR spectra throughout the synthesis of RhMn@SiO_2 starting from the second grafting. (c) Particle size distribution and TEM images of RhMn@SiO_2.

The metal loadings in RhMn@SiO_2 and Rh@SiO_2, analyzed by inductively coupled plasma optical emission spectroscopy (ICP-OES), are similar with *ca.* 2.3 wt% Rh. The RhMn@SiO_2 also contains 1.45 wt% Mn, which corresponds to a *ca.* 1 : 1 molar ratio of Rh : Mn (Table S1†). We also carried out H_2 and CO chemisorption to better characterize the surface state of Rh (Table S1, Fig. S14 and S15†). The H_2 and CO uptake found RhMn@SiO_2 are both higher than that for Rh@SiO_2, implying that the Rh nanoparticles are smaller in the presence of the Mn promoter. Note that H_2/CO chemisorption is not effective for estimating the metal dispersion in the case of Rh due to the multiple adsorption of hydrogen and the complicated CO adsorption modes.[25,26]

Furthermore, FTIR spectra of adsorbed CO under different CO pressures reveal that the adsorption of CO on both Rh@SiO_2 and RhMn@SiO_2 is irreversible, indicating a strong CO adsorption, consistent with previous reports (Fig. S16†).[26] In addition, in both cases, the IR bands are red-shifted by *ca.* 10 cm^{-1} after the evacuation likely indicating a decrease in dipole–dipole interaction at lower CO coverage.[26] At a CO pressure of 2.4 mbar, two bands at around 2070 and 1890 cm^{-1} are observed upon subtraction of the background for both materials; they are attributed to linearly bound CO and bridged CO adsorbed on metallic Rh, respectively (Fig. S17†).[27,28] Note that bands at 2080 and 2010 cm^{-1}, commonly attributed to the geminal dicarbonyl on Rh^+ sites ($Rh\text{-}(CO)_2$), are not observed, indicating that the grafted Rh^I species are completely reduced to Rh(0) metal after H_2 treatment.[29,30]

Catalyst evaluation for CO_2 hydrogenation

The catalytic performances of Rh@SiO_2 and RhMn@SiO_2 were tested at 230 °C under 40 bar ($H_2/CO_2/Ar = 3:1:1$). Following exposure to air, the catalyst was reduced at 400 °C under H_2 (1 bar, 50 mL min^{-1}) prior to CO_2 hydrogenation. The CO_2 conversion was maintained below 10% for kinetic consideration. Under these conditions, CH_4 is the main product for Rh@SiO$_2$ along with a small fraction of CO across a wide range of CO_2 conversion (Fig. 2a and S18†), consistent with earlier reports on monometallic Rh catalysts during CO_x (CO and CO_2) hydrogenation in the absence of promoter.[6,31,32] Upon the introduction of Mn as a promoter, the product selectivity significantly shifts to a mixture of CH_4, CO, CH_3OH, and CH_3CH_2OH (Fig. 2b and S19†). Note that Mn@SiO$_2$ was also tested under identical conditions and showed no activity in CO_2 hydrogenation. This rules out that the products such as CO and CH_3OH are formed directly over the Mn promoter.

In addition, the CO selectivity and methanol selectivity on the RhMn@SiO$_2$ catalyst gradually decrease with the increase in CO_2 conversion, while the CH_4 selectivity shows the opposite trend. This indicates that CO and CH_3OH are further hydrogenated to CH_4 with increased contact time. When the flow rate was set at 50 mL min^{-1}, we compared the formation rate of products of Rh@SiO$_2$ and RhMn@SiO$_2$. As shown in Fig. 2c, the formation rate of CH_4 on Rh@SiO$_2$ (6.62 g g$_{Rh}^{-1}$ h^{-1}) is higher than that of RhMn@SiO$_2$ (1.83 g g$_{Rh}^{-1}$ h^{-1}) by a factor of around 3.5. Moreover, the formation rate of CO, CH_3OH, and CH_3CH_2OH on RhMn@SiO$_2$ is 1.75 g g$_{Rh}^{-1}$ h^{-1}, 0.50 g g$_{Rh}^{-1}$ h^{-1} and 0.10 g g$_{Rh}^{-1}$ h^{-1} respectively. Therefore, these catalytic results clearly show that the introduction of the Mn promoter significantly affects the methanation reaction, while promoting the formation of CO, CH_3OH, and CH_3CH_2OH.

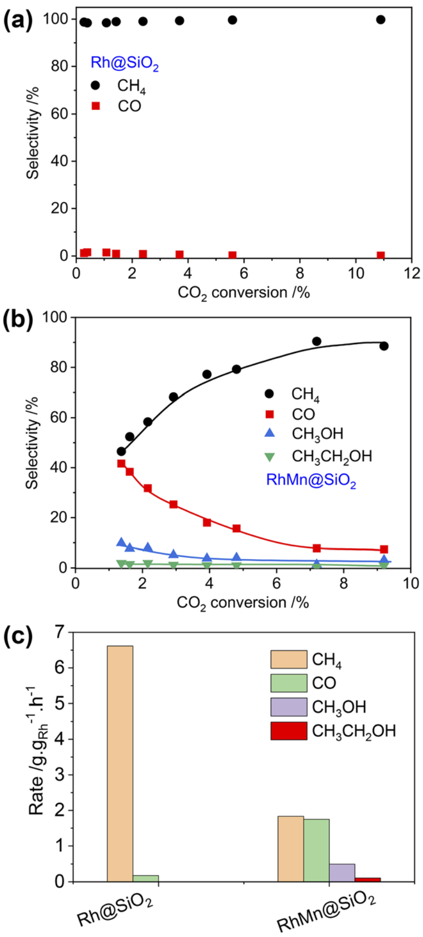

Fig. 2 Product selectivity *vs.* CO_2 conversion for Rh@SiO$_2$ (a) and RhMn@SiO$_2$ (b). Reaction conditions: 30 mg for Rh@SiO$_2$, 125 mg for RhMn@SiO$_2$, $F = 6–100$ mL min^{-1}, $T = 230$ °C, $P = 40$ bar. (c) Product formation rate on Rh@SiO$_2$ and RhMn@SiO$_2$ at a flow rate of 50 mL min^{-1}.

In situ X-ray absorption spectroscopy

To gain further insight into the structure of the catalysts under different conditions, *in situ* XAS was performed on both Rh@SiO$_2$ and RhMn@SiO$_2$, at both the Rh and Mn K-edges (Fig. S20†). The catalyst structures of the material as prepared (exposed to air), reduced and post-CO_2 hydrogenation were studied by extended X-ray absorption fine structure (EXAFS), while any changes in the chemical state in the duration of H_2 reduction and CO_2 hydrogenation were studied by X-ray absorption near edge structure (XANES). We first investigated the evolution of the structure of Rh@SiO$_2$ and RhMn@SiO$_2$ catalysts under different conditions from the Rh K-edge (Fig. 3 and 4). The corresponding best-fit details are shown in Fig. S21–S27, Tables S2 and S3.† Compared to the XANES spectra of Rh and Rh_2O_3 references, the XANES spectra of Rh@SiO$_2$ after exposure to air closely match that of metallic Rh (Fig. 3a). Furthermore, only one peak at 2.4 Å corresponding to the contribution of Rh–Rh scattering path appears in the Fourier transforms of EXAFS spectra combined with the fitting results (Fig. 3b, and S22–S24†). These results indicate that Rh in the as-synthesized Rh@SiO$_2$ catalyst is exclusively present in a metallic

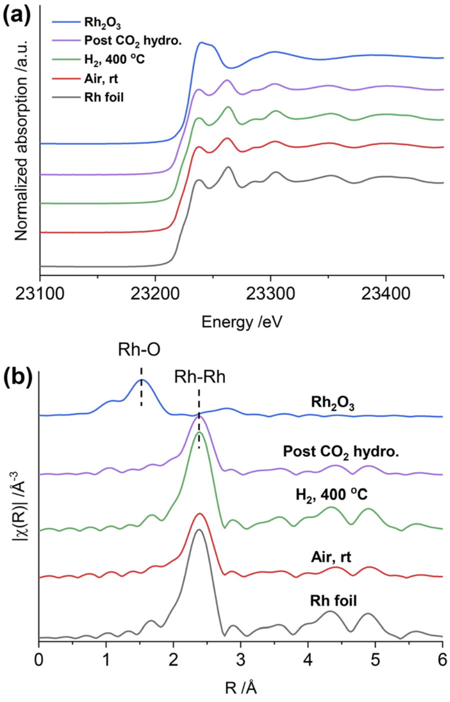

Fig. 3 *In situ* Rh K-edge XANES spectra (a) and the k^2-weighted Fourier transforms of EXAFS spectra (b) of the Rh@SiO$_2$ catalyst under different conditions and reference samples.

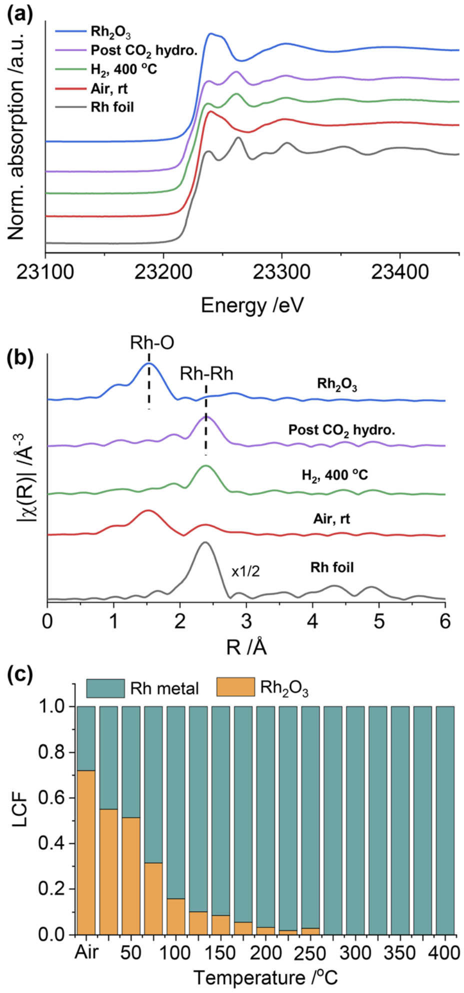

Fig. 4 *In situ* Rh K-edge XANES spectra (a) and the k^2-weighted Fourier transforms of EXAFS spectra (b) of the RhMn@SiO$_2$ catalyst under different conditions and reference samples. (c) Results of linear combination fitting (LCF) of Rh K-edge XANES.

state, even upon exposure to air. After H$_2$ reduction, the average coordination number (CN) in the first Rh–Rh shell increases from 8.9 to 10.1 (Table S3†), suggesting that the size of Rh particles grows in the reduced sample. Of interest, the CN was reduced to 8.7 after the CO$_2$ hydrogenation, indicating that a re-dispersion of Rh nanoparticles may occur during the reaction. This is consistent with earlier reports that show that CO species formed from CO$_2$ hydrogenation can generate carbonyl species and induce the re-dispersion of Rh particles.[33] Therefore, we consider that the same re-dispersion of Rh particles likely occurs on Rh@SiO$_2$ due to the formation of Rh carbonyl species during the reaction.

Regarding RhMn@SiO$_2$, the edge position and white line intensity of air-exposed XANES spectra are more similar to that of the Rh$_2$O$_3$ reference, indicating that Rh is oxidized in such materials (Fig. 4a). The main peak in the Fourier transform of EXAFS spectra is at 1.5 Å, attributed to the contribution of the Rh–O scattering path (Fig. 4b). The EXAFS spectra were modeled using Rh–O (2.03 Å) and Rh–Rh (2.68 Å) scattering paths, showing a CN of 4.5 and 2.2 for Rh–O and Rh–Rh, respectively (Table S3, Fig. S25†). Therefore, the air-exposed RhMn@SiO$_2$ mainly contains oxidized Rh species with a small amount of metallic Rh. After H$_2$ reduction at 400 °C, the edge position shifts to lower energy, the white line intensity decreases, and the characteristic peak at 23 262 eV belonging to metallic Rh appears. In addition, the peak at 1.5 Å completely disappears while the intensity of the peak at 2.4 Å increases markedly. No Rh–O and Rh–Mn features were observed in either XANES and Fourier transforms of EXAFS spectra, which indicates that the oxidized Rh was fully reduced to metallic Rh with no alloy formation. No significant change in the CN of the RhMn@SiO$_2$ catalyst is observed post-CO$_2$ hydrogenation compared to that of the reduced RhMn@SiO$_2$. Notably, the CN of reduced RhMn@SiO$_2$ (6.4) is less than that found in reduced Rh@SiO$_2$ (10.1) consistent with the presence of smaller metal particles, resulting in lower average CN.[34] This is consistent with the presence of smaller particle size in RhMn@SiO$_2$ than in Rh@SiO$_2$ as observed by TEM. Compared to the pure Rh@SiO$_2$ the chemical state of Rh in air-exposed RhMn@SiO$_2$ is quite distinct, suggesting that the oxidation of Rh is induced by the presence of Mn.

As described above, the chemical state of Rh in the RhMn@SiO$_2$ sample was dramatically changed after H$_2$ reduction. Therefore, the XANES spectra were further collected to monitor the subtle changes during H$_2$ temperature programmed reduction (H$_2$-TPR) (Fig. S28†). The XANES spectra were analyzed by linear combination fitting (LCF). To minimize the influence of particle size, we employ Rh@SiO$_2$ as the standard Rh metal spectra (Fig. 4c and S29†). The air-exposed RhMn@SiO$_2$ sample contains approximately a 70 : 30 mixture of Rh$_2$O$_3$ and Rh metal phases. When the temperature is increased to 200 °C, the spectra match well with the Rh metal spectra, and there are no obvious changes on further increasing the temperature. Therefore, the Rh oxide in RhMn@SiO$_2$ can be completely reduced at around 200 °C. In contrast, there is no chemical state change observed for Rh in the Rh@SiO$_2$ sample during the H$_2$-TPR (Fig. S30†).

We also collected the *in situ* Mn K-edge XAS spectra under identical conditions. As shown in Fig. 5a, compared to the Mn^{II}@SiO$_2$, the edge position of air-exposed RhMn@SiO$_2$ shifts to a higher position, suggesting that the pristine Mn^{II} is oxidized upon exposure to air. We further quantify the average oxidation state of the Mn by establishing a calibration curve describing the relationship between the oxidation state and the difference in edge energy (Fig. 5b and S31†).[35] The evaluated average oxidation state of Mn in air-exposed RhMn@SiO$_2$ is +2.6. Due to the proximity between Mn sites and Rh nanoparticles, we speculate that the oxidation of Mn enables to induce the oxidation of Rh (confirmed from the Rh K-edge spectra), probably resulting in the formation of Mn–O–Rh interfaces. After the H$_2$ reduction at 400 °C, the edge position shifts back to lower energy, which is similar to that of the Mn^{II}@SiO$_2$ standard, indicating that the oxidized Mn is reduced back to Mn^{II}. The Fourier transforms of Mn K-edge EXAFS spectra were analyzed, and references (Mn@SiO$_2$, MnO, and Mn foil) are employed for comparison (Fig. S32†). We can see that the peak of RhMn@SiO$_2$ post-H$_2$ reduction or CO$_2$ hydrogenation is similar to that of Mn@SiO$_2$-air free, and there is no Mn–Mn peak observed. It is suggested that Mn in RhMn@SiO$_2$ catalyst

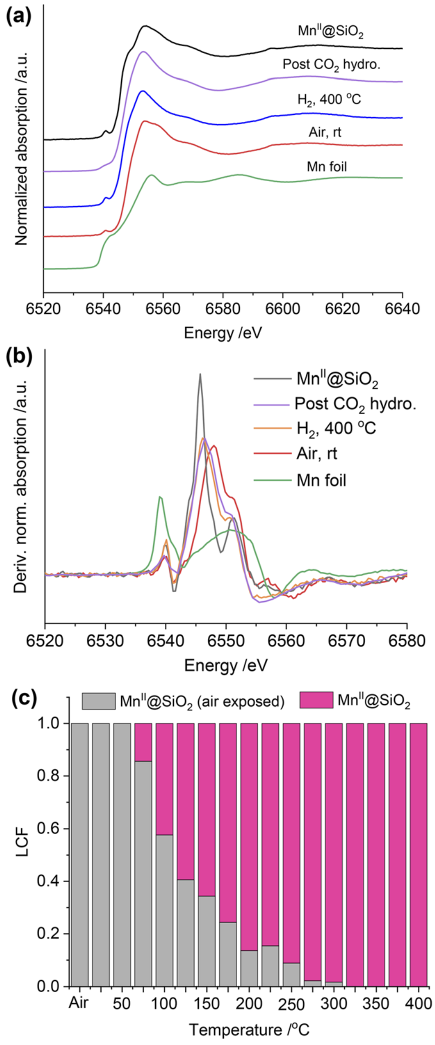

Fig. 5 (a) *In situ* Mn K-edge XANES spectra of RhMn@SiO$_2$ under different conditions and reference. (b) The first derivative of the EXAFS spectra at the Mn K-edge of RhMn@SiO$_2$ under different conditions and reference samples. (c) Results of linear combination fitting (LCF) of Mn K-edge XANES.

remains atomically dispersed on SiO$_2$, while no sintering or alloying occurs during the H$_2$ reduction and CO$_2$ hydrogenation.

The Mn K-edge XANES spectra were also recorded to monitor the chemical changes of Mn during the H$_2$ temperature programmed reduction (Fig. S33†). Because Mn in RhMn@SiO$_2$ is mostly isolated (*vide supra*), we employed the air-free and air-exposed Mn^{II}SiO$_2$ samples as the references for the linear combination fitting, which enables to obtain a good fitting (Fig. S34†). As shown in Fig. 5c, the oxidized Mn starts to resemble Mn^{II}@SiO$_2$ at around 75 °C and was completely transformed to Mn^{II} at around 300 °C. The reduced temperature is about 100 °C higher than that of Rh (200 °C). This is because the oxygen affinity of Mn is higher than that of Rh, making Mn more difficult to reduce.

Upon exposing the catalyst to CO$_2$ hydrogenation reaction conditions at 20 bar (H$_2$/CO$_2$/Ar = 1 : 3 : 1), we observed the alterations in both Mn K-edge and Rh K-edge XANES spectra with time on stream (Fig. S35† and 6a and b). The edge position gradually shifts to higher energy for both Mn K-edge and Rh K-edge XANES spectra during CO$_2$ hydrogenation, with slight changes in the white line intensity of both (Fig. S35†). These transformations are consistent with the partial oxidation of Mn and Rh under CO$_2$ hydrogenation conditions. However, we did not observe any changes when comparing the XANES spectra before and post-CO$_2$ hydrogenation for the pure Rh@SiO$_2$ catalyst (Fig. S36†). These changes in Rh are thereby induced by the Mn promoter during CO$_2$ hydrogenation and correlate with suppressing the methanation reaction and promoting the formation of CO and alcohols.

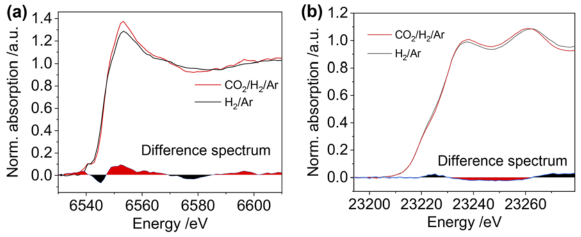

Fig. 6 The *in situ* Mn K-edge XANES spectra (a) and Rh K-edge XANES spectra (b) of the RhMn@SiO$_2$ catalyst collected under H$_2$/Ar (3 : 2, 20 bar) (black line) and under CO$_2$/H$_2$/Ar (1 : 3 : 1, 20 bar) after the reaction of 2 h (red line). The difference spectra between these two spectra are shown at the bottom of the respective spectra.

To gain insight into the surface-adsorbed species, *in situ* DRIFTS studies were carried out over Rh@SiO$_2$ and RhMn@SiO$_2$ at 20 bar and 230 °C. Upon switching to CO$_2$/H$_2$/Ar (1 : 3 : 1) gas, IR bands at 1294, 2050, and 2170 cm^{-1} were observed over the Rh@SiO$_2$ catalyst, these bands are attributed to adsorbed bidentate carbonate (CO$_3^*$), absorbed CO* and gaseous CO, respectively (Fig. 7a).[36,37] In parallel, adsorbed CH$_x$ species and gaseous CH$_4$ were detected, as evidenced by the signals at 2856/2956 cm^{-1} and 3015 cm^{-1}, respectively.[6,38]

The same *in situ* DRIFTS studies for RhMn@SiO$_2$ also demonstrated the presence of adsorbed bidentate CO$_3^*$ (band at 1294 cm^{-1}), CO* (band at 2050 cm^{-1}), and CH$_x^*$ (bands at 2856 and 2956 cm^{-1}) species (Fig. 7b). However, in contrast to Rh@SiO$_2$, the bands for formate species (1591 and 2874 cm^{-1}), a key intermediate for methanol formation, were observed over RhMn@SiO$_2$.[39] Moreover, the intensity of the band for gaseous CH$_4$ over RhMn@SiO$_2$ is significantly lower than that of RhMn@SiO$_2$, while the intensity of the band for gaseous CO is much higher. These observations are in line with our CO$_2$ hydrogenation results, where the presence of Mn enables to minimize the methanation reaction and promote the formation of CO and CH$_3$OH.

Based on the *in situ* XAS and DRIFTS experiments, we propose a possible mechanism to illustrate the promotional effect of Mn for Rh-based catalysts. After being exposed to air, the Mn^{II} is oxidized (average oxidation state is +2.6) in the vicinity of Rh and promotes Rh oxidation. This likely leads to the formation of Mn–O–Rh interfaces due to the proximity between the isolated Mn and Rh nanoparticles, driving the partial oxidation of Rh. It is accepted that the CH$_4$ comes from the dissociative activation of C═O on the

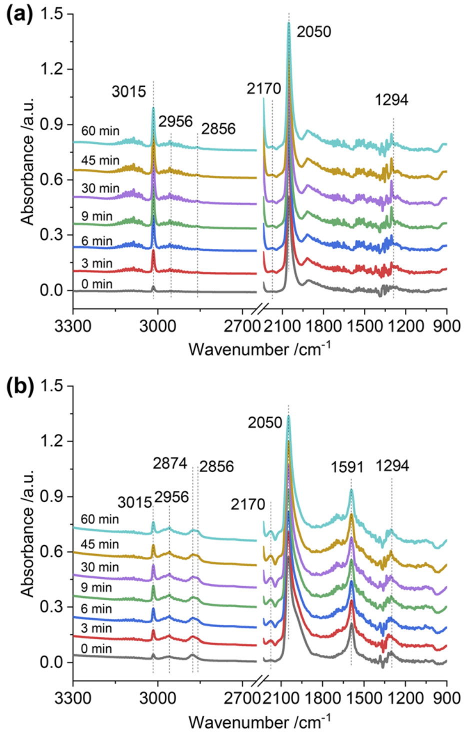

Fig. 7 *In situ* DRIFTS spectra of adsorbed species on Rh@SiO_2 (a) and RhMn@SiO_2 (b) collected under CO_2/H_2/Ar (1 : 3 : 1, 20 bar).

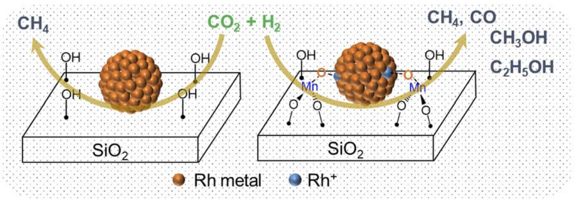

Fig. 8 The scheme for CO_2 hydrogenation over Rh@SiO_2 and RhMn@SiO_2 catalysts.

Rh^0 site, while the CO and methanol are produced from the non-dissociative activation of C═O on the Rh^+ site.[5] Therefore, the pure Rh@SiO_2 presenting only the metallic state of Rh under CO_2 hydrogenation is a methanation catalyst, However, the presence of Mn induces the formation of the Rh–O–Mn interface to maintain the Rh^+ site, which is in parallel with the stabilization of formate species as evidenced by *in situ* DRIFTS, thus promoting the formation of CO and alcohols and the suppression of methanation activity (Fig. 8).

Conclusions

In summary, we employed the SOMC/TMP approach to construct well-defined Rh-based catalysts (RhMn@SiO_2 and Rh@SiO_2) in order to study the promotional effect of Mn for CO_2 hydrogenation. We find that the presence of Mn not only decreases particle size but also dramatically suppresses methanation. The product can be steered from CH_4 on non-Mn-promoted Rh@SiO_2 to a mixture of methane and oxygenates (CO and CH_3OH along with little CH_3CH_2OH) on RhMn@SiO_2. *In situ* XAS reveals that the isolated Mn remains atomically dispersed in the vicinity of Rh nanoparticles during either the H_2 pretreatment or CO_2 hydrogenation. This excludes the formation of mixed oxides or alloys as the major contributors to the activity of these catalysts. The presence of Mn^{II} in the vicinity of Rh nanoparticles enables to drive the oxidation of Rh, likely generating Mn–O–Rh interfaces under reaction conditions. The formed interface is proposed to be key to maintaining Rh^+ sites, which is responsible for suppressing the methanation reaction and stabilizing the formate species as evidenced by *in situ* DRIFTS to promote the formation of CO and alcohols. These observations reveal how the Mn promoter dynamically influences Rh nanoparticles, thereby steering the product selectivity. This study provides insights into the rational design of catalysts for CO_2 hydrogenation.

Data availability

We do not have more experimental and computational data associated with this article.

Author contributions

Z. W. and C. C. conceived and designed the study. C. C. supervised the project. Z. W. performed the catalyst preparation, characterization, and catalytic reactions. C. E. developed the Rh precursor, S. D., X. Z. and C. E. assisted in *in situ* XAS experiment. W. Z. and C. C. co-wrote the manuscript. All authors discussed the results and commented on the manuscript.

Conflicts of interest

There are no conflicts to declare.

Acknowledgements

C. C., W. Z. and X. Z. acknowledge the National Centre of Competence in Research (NCCR) Catalysis (grant 180544) for financial support. C. C. and S. R. D. acknowledge the Swiss National Science Foundation (grants 200021_169134, and 200020B_192050), while C. E. acknowledges the Swiss National Science Foundation (grant 200020B_192050) and the Scholarship Fund of the Swiss Chemical Industry (SSCI). The authors acknowledge Dr W. V. Beek and Dr D. Stoian at the Swiss Norwegian Beamlines (SNBL, ESRF) for the provision of beamtime and support with *in situ* XAS experiments *via* proposal A31-1-168. Furthermore, ScopeM is gratefully acknowledged for their support and assistance in this work through project No. 2460. The authors thank Dr Y. Wang for assistance with *in situ* DRIFTS. The authors also thank C. Hansen and C. J. Kaul for assistance with X-ray crystallography and ss-NMR, respectively. Crystal Data for Li(DIA)(THF) and Rh(COD)(DIA) can be obtained free of charge from the Cambridge Crystallographic Data Centre (CCDC number: 2237587 and 2237586†).

Notes and references

1 G. A. Olah, G. K. Prakash and A. Goeppert, *J. Am. Chem. Soc.*, 2011, **133**, 12881–12898.

2 E. S. Sanz-Pérez, C. R. Murdock, S. A. Didas and C. W. Jones, *Chem. Rev.*, 2016, **116**, 11840–11876.

3 W. Zhou, K. Cheng, J. Kang, C. Zhou, V. Subramanian, Q. Zhang and Y. Wang, *Chem. Soc. Rev.*, 2019, **48**, 3193–3228.

4 X. Jiang, X. Nie, X. Guo, C. Song and J. G. Chen, *Chem. Rev.*, 2020, **120**, 7984–8034.

5 D. Xu, Y. Wang, M. Ding, X. Hong, G. Liu and S. C. E. Tsang, *Chem*, 2021, **7**, 849–881.

6 F. Zhang, W. Zhou, X. Xiong, Y. Wang, K. Cheng, J. Kang, Q. Zhang and Y. Wang, *J. Phys. Chem. C*, 2021, **125**, 24429–24439.

7 H. Kusama, K. Okabe, K. Sayama and H. Arakawa, *Energy*, 1997, **22**, 343–348.

8 M. R. Gogate and R. J. Davis, *Catal. Commun.*, 2010, **11**, 901–906.

9 G. Wang, R. Luo, C. Yang, J. Song, C. Xiong, H. Tian, Z.-J. Zhao, R. Mu and J. Gong, *Sci. China: Chem.*, 2019, **62**, 1710–1719.

10 C. Yang, R. Mu, G. Wang, J. Song, H. Tian, Z. J. Zhao and J. Gong, *Chem. Sci.*, 2019, **10**, 3161–3167.

11 M. Suvarna, P. Preikschas and J. Pérez-Ramírez, *ACS Catal.*, 2022, **12**, 15373–15385.

12 C. Copéret, A. Comas-Vives, M. P. Conley, D. P. Estes, A. Fedorov, V. Mougel, H. Nagae, F. Nunez-Zarur and P. A. Zhizhko, *Chem. Rev.*, 2016, **116**, 323–421.

13 C. Copéret, *Acc. Chem. Res.*, 2019, **52**, 1697–1708.

14 J. Meyet, A. Ashuiev, G. Noh, M. A. Newton, D. Klose, K. Searles, A. P. van Bavel, A. D. Horton, G. Jeschke, J. A. van Bokhoven and C. Copéret, *Angew. Chem., Int. Ed.*, 2021, **60**, 16200–16207.

15 S. R. Docherty, L. Rochlitz, P.-A. Payard and C. Copéret, *Chem. Soc. Rev.*, 2021, **50**, 5806–5822.

16 L. Rochlitz, Q. Pessemesse, J. W. A. Fischer, D. Klose, A. H. Clark, M. Plodinec, G. Jeschke, P.-A. Payard and C. Copéret, *J. Am. Chem. Soc.*, 2022, **144**, 13384–13393.

17 S. R. Docherty and C. Copéret, *J. Am. Chem. Soc.*, 2021, **143**, 6767–6780.

18 E. Lam, J. J. Corral-Pérez, K. Larmier, G. Noh, P. Wolf, A. Comas-Vives, A. Urakawa and C. Copéret, *Angew. Chem., Int. Ed.*, 2019, **58**, 13989–13996.

19 E. Lam, G. Noh, K. Larmier, O. V. Safonova and C. Copéret, *J. Catal.*, 2021, **394**, 266–272.

20 E. Lam, G. Noh, K. W. Chan, K. Larmier, D. Lebedev, K. Searles, P. Wolf, O. V. Safonova and C. Copéret, *Chem. Sci.*, 2020, **11**, 7593–7598.

21 G. Noh, E. Lam, D. T. Bregante, J. Meyet, P. Šot, D. W. Flaherty and C. Copéret, *Angew. Chem., Int. Ed.*, 2021, **60**, 9650–9659.

22 E. Lam, K. Larmier, P. Wolf, S. Tada, O. V. Safonova and C. Copéret, *J. Am. Chem. Soc.*, 2018, **140**, 10530–10535.

23 S. R. Docherty, N. Phongprueksathat, E. Lam, G. Noh, O. V. Safonova, A. Urakawa and C. Copéret, *JACS Au*, 2021, **1**, 450–458.

24 B. Ghaffari, J. Mendes-Burak, K. W. Chan and C. Copéret, *Chem.–Eur. J.*, 2019, **25**, 13869–13873.

25 B. J. Kip, F. B. M. Duivenvoorden, D. C. Koningsberger and R. Prins, *J. Catal.*, 1987, **105**, 26–38.

26 G. Prieto, P. Concepción, A. Martínez and E. Mendoza, *J. Catal.*, 2011, **280**, 274–288.

27 S. Chuang, R. Stevens and R. Khatri, *Top. Catal.*, 2005, **32**, 225–232.

28 N. Yang, J. S. Yoo, J. Schumann, P. Bothra, J. A. Singh, E. Valle, F. Abild-Pedersen, J. K. Nørskov and S. F. Bent, *ACS Catal.*, 2017, **7**, 5746–5757.

29 V. Schwartz, A. Campos, A. Egbebi, J. J. Spivey and S. H. Overbury, *ACS Catal.*, 2011, **1**, 1298–1306.

30 F. C. Meunier, *J. Phys. Chem. C*, 2021, **125**, 21810–21823.

31 H. Kusama, K. Okabe, K. Sayama and H. Arakawa, *Catal. Today*, 1996, **28**, 261–266.

32 H. T. Luk, C. Mondelli, D. C. Ferré, J. A. Stewart and J. Pérez-Ramírez, *Chem. Soc. Rev.*, 2017, **46**, 1358–1426.

33 H. Kusama, K. K. Bando, K. Okabe and H. Arakawa, *Appl. Catal., A*, 2000, **197**, 255–268.

34 A. M. Beale and B. M. Weckhuysen, *Phys. Chem. Chem. Phys.*, 2010, **12**, 5562–5574.

35 A. Campos, N. Lohitharn, A. Roy, E. Lotero, J. G. Goodwin and J. J. Spivey, *Appl. Catal., A*, 2010, **375**, 12–16.

36 D. Xu, M. Ding, X. Hong, G. Liu and S. C. E. Tsang, *ACS Catal.*, 2020, **10**, 5250–5260.

37 H. Du, C. T. Williams, A. D. Ebner and J. A. Ritter, *Chem. Mater.*, 2010, **22**, 3519–3526.

38 C. Wang, E. Guan, L. Wang, X. Chu, Z. Wu, J. Zhang, Z. Yang, Y. Jiang, L. Zhang, X. Meng, B. C. Gates and F. Xiao, *J. Am. Chem. Soc.*, 2019, **141**, 8482–8488.

39 Y. Wang, S. Kattel, W. Gao, K. Li, P. Liu, J. G. Chen and H. Wang, *Nat. Commun.*, 2019, **10**, 1166.